

Fracture interface waves

Boliang Gu¹

Department of Materials Science and Mineral Engineering, University of California, Berkeley

Kurt T. Nihei and Larry R. Myer

Earth Sciences Division, Lawrence Berkeley Laboratory, Berkeley, California

Laura J. Pyrak-Nolte

Department of Civil Engineering and Geological Sciences, University of Notre Dame, Notre Dame, Indiana

Abstract. Interface waves on a single fracture in an elastic solid are investigated theoretically and numerically using plane wave analysis and a boundary element method. The finite mechanical stiffness of a fracture is modeled as a displacement discontinuity. Analysis for inhomogeneous plane wave propagation along a fracture yields two dispersive equations for symmetric and antisymmetric interface waves. The basic form of these equations are similar to the classic Rayleigh equation for a surface wave on a half-space, except that the displacements and velocities of the symmetric and antisymmetric fracture interface waves are each controlled by a normalized fracture stiffness. For low values of the normalized fracture stiffness, the symmetric and antisymmetric interface waves degenerate to the classic Rayleigh wave on a traction-free surface. For large values of the normalized fracture stiffness, the antisymmetric and symmetric interface waves become a body *S* wave and a body *P* wave, respectively, which propagate parallel to the fracture. For intermediate values of the normalized fracture stiffness, both interface waves are dispersive. Numerical modeling performed using a boundary element method demonstrates that a line source generates a *P*-type interface wave, in addition to the two Rayleigh-type interface waves. The magnitude of the normalized fracture stiffness is observed to control the velocities of the interface waves and the partitioning of seismic energy among the various waves near the fracture.

Introduction

At the microscale, a fracture in rock appears as two surfaces of irregular topography which contact to form void spaces and asperities of contact. A fracture with a sparse population of asperities is more compliant than a fracture with closely spaced asperities [Greenwood and Williamson, 1966; Gangi, 1978; Brown and Scholz, 1985; Hopkins *et al.*, 1987; Cook, 1992]. It has been observed that the additional compliance of a fracture results in a variety of interesting elastic wave phenomena. For example, laboratory transmission measurements of normally incident *P* and *S* waves across a fracture exhibit low-pass filtering of the source wavelet accompanied by a small travel time delay [Pyrak-Nolte *et al.*, 1990]. In addition, laboratory measurements of elastic wave propagation parallel to a fracture have revealed that a fracture can support dispersive interface waves [Pyrak-Nolte *et al.*, 1992]. In both sets of experiments, the amplitude and velocity of the waves propagating across or along a

fracture were observed to be sensitive to the magnitude of the mechanical stiffness of the fracture or, equivalently, to the static stress imposed on the fracture.

Murty [1975] examined the condition for the existence of an interface wave on a nonwelded interface with a discontinuity in shear displacement across the thickness of the interface. Pyrak-Nolte and Cook [1987] extended Murty's analysis to the case where both normal and shear displacements are discontinuous across a nonwelded interface. They found that a single nonwelded interface, such as fracture, can support a fast (symmetric) wave and a slow (antisymmetric) wave which propagate with phase velocities between the Rayleigh and shear wave velocities and are dispersive. Recent laboratory measurements by Pyrak-Nolte *et al.* [1992] have confirmed the existence of the fast and slow interface waves in a synthetic fracture in aluminum. Very good agreement was found between the measured and predicted group velocities of the fast and slow interface waves. In the field of nondestructive evaluation, the displacement discontinuity model has been used to approximate thin elastic adhesive bonds [e.g., Rokhlin, 1984; Xu and Datta, 1990]. In these models, shear displacements across the thin bond are discontinuous by an amount that is inversely proportional to the shear stiffness of the bond while normal displacements are continuous, as in the case of Murty's [1975] model.

¹ Now at Earth Sciences Division, Lawrence Berkeley Laboratory, Berkeley, California.

Copyright 1996 by the American Geophysical Union.

Paper number 95JB02846.
0148-0227/96/95JB-02846\$05.00

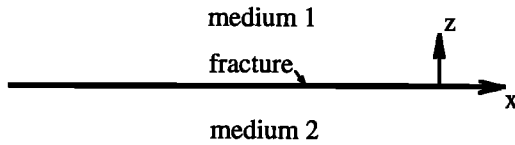


Figure 1. Problem geometry used in the derivation of interface wave equations.

This paper investigates interface waves on a planar fracture in an elastic solid using plane wave and numerical analysis. The fracture is modeled as a displacement discontinuity boundary condition in both shear and normal displacements. Closed-form equations for fracture interface waves are developed. The characteristics of the dispersion and particle motions of trapped and leaky interface waves are examined. The partitioning of seismic energy among waves near the fracture is also evaluated.

Plane Wave Analysis

The seismic behavior of a thin fracture compared to the wavelength can be well described by the displacement discontinuity model. Across such a discontinuity, seismic stresses are continuous and particle displacements are discontinuous by an amount which is determined by the ratio of the stress on the fracture surface to the fracture specific stiffness [Kendall and Tabor, 1971; Schoenberg, 1980; Rokhlin and Wang, 1991; Cook, 1992]. This boundary condition degenerates to that for a welded fracture as the fracture specific stiffness approaches infinity and, for two traction-free surfaces, as the fracture specific stiffness reaches zero. The displacement discontinuity model was found to accurately predict the frequency-dependent transmission of a plane wave normally incident upon a fracture [Schoenberg, 1980; Myer et al., 1985] and the existence of interface waves along a fracture [Pyrak-Nolte and Cook, 1987].

Consider a fracture located in the x - y plane, as shown in Figure 1. The displacement discontinuity boundary conditions for in-plane motion (P and SV waves) are

$$\begin{aligned} u_1 - u_2 &= \tau_{xz1}/k_x, \\ w_1 - w_2 &= \tau_{zz1}/k_z, \\ \tau_{zx1} &= \tau_{zx2}, \\ \tau_{zz1} &= \tau_{zz2}, \end{aligned} \tag{1}$$

where u and w are the x and z components of the particle displacement, τ_{zx} and τ_{zz} are the shear and normal stresses

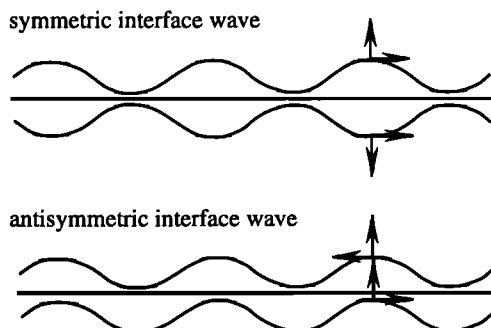


Figure 2. Schematic of symmetric and antisymmetric interface waves.

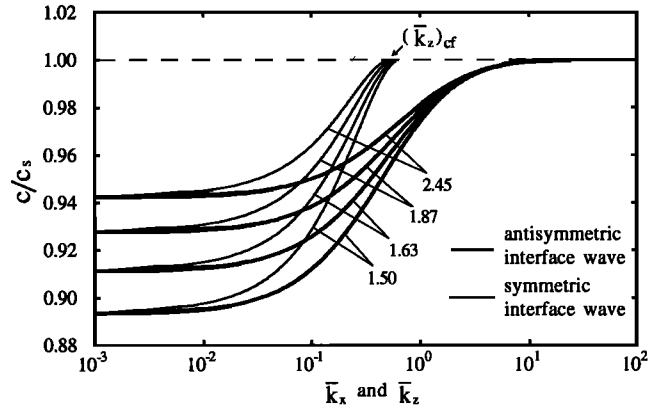


Figure 3. Normalized phase velocities of the symmetric and antisymmetric interface waves as a function of the normalized fracture stiffness for a range of C_P/C_S ratios. The numbers of 1.50, 1.63, 1.87, and 2.45 labeled on the curves are the C_P/C_S ratios, which are equivalent to Poisson's ratios of 0.1, 0.2, 0.3 and 0.4, correspondingly. Symbol $(\bar{k}_z)_{cf}$ is the cut-off normalized fracture stiffness above which the symmetric interface wave ceases to exist in the normal mode.

on the fracture surfaces, k_x and k_z are the x and z components of the fracture specific stiffness, and subscripts 1 and 2 refer to the media above and below the fracture, respectively.

The generalized potentials for an inhomogeneous plane wave propagating in the x direction with exponentially decaying amplitude in the z direction can be expressed as

$$\begin{aligned} \phi_1 &= A_1 e^{-p\omega z} e^{i\omega(x/C-t)}, \quad z \geq 0 \\ \phi_2 &= A_2 e^{p\omega z} e^{i\omega(x/C-t)}, \quad z \leq 0 \end{aligned} \tag{2}$$

for P wave motion and

$$\begin{aligned} \psi_1 &= B_1 e^{-q\omega z} e^{i\omega(x/C-t)}, \quad z \geq 0 \\ \psi_2 &= B_2 e^{q\omega z} e^{i\omega(x/C-t)}, \quad z \leq 0 \end{aligned} \tag{3}$$

for SV wave motion, where $i = \sqrt{-1}$, ω is the angular frequency, t is time, A_1 , A_2 , B_1 , and B_2 are undetermined constants, C is the phase velocity of the inhomogeneous wave, and p and q are defined as

$$\begin{aligned} p &= \sqrt{\frac{1}{C^2} - \frac{1}{C_P^2}}, \\ q &= \sqrt{\frac{1}{C^2} - \frac{1}{C_S^2}}, \end{aligned} \tag{4}$$

where C_P and C_S are the P and S wave velocities, respectively.

Using the potentials in (2) and (3) and the Helmholtz theorem,

$$\begin{aligned} u &= \frac{\partial \phi}{\partial x} - \frac{\partial \psi}{\partial z}, \\ w &= \frac{\partial \phi}{\partial z} + \frac{\partial \psi}{\partial x}, \end{aligned} \tag{5}$$

the particle displacements are derived with the form

$$\begin{aligned} u_1 &= \omega \left[i \frac{1}{C} A_1 e^{-p\omega z} + q B_1 e^{-q\omega z} \right] e^{i\omega(x/C-t)}, \\ w_1 &= \omega \left[-p A_1 e^{-p\omega z} + i \frac{1}{C} B_1 e^{-q\omega z} \right] e^{i\omega(x/C-t)}, \end{aligned} \tag{6}$$

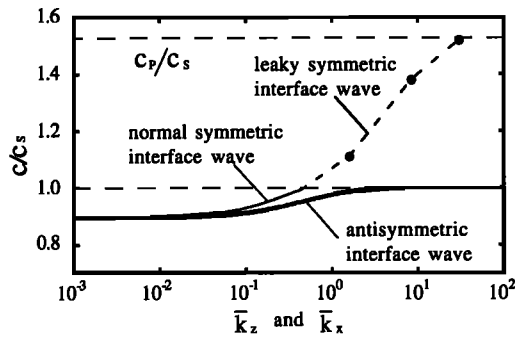


Figure 4. Normalized phase velocities of the symmetric and antisymmetric interface waves, including the leaky mode of the symmetric interface wave, as a function of the normalized fracture stiffness when $C_p/C_s=1.53$.

for the upper medium and

$$u_2 = \omega \left[i \frac{1}{C} A_2 e^{p\omega z} - q B_2 e^{q\omega z} \right] e^{i\omega(x/C-t)}, \quad (7)$$

$$w_2 = \omega \left[p A_2 e^{p\omega z} + i \frac{1}{C} B_2 e^{q\omega z} \right] e^{i\omega(x/C-t)},$$

for the lower medium.

Seismic stresses in the upper and lower media obtained from (6) and (7) and Hooke's Law are

$$\tau_{zx1} = \omega^2 \left[-\frac{2ip\mu}{C} A_1 e^{-p\omega z} - \mu \left(\frac{1}{C^2} + p^2 \right) B_1 e^{-q\omega z} \right] e^{i\omega(x/C-t)},$$

$$\tau_{zz1} = \omega^2 \left[\mu \left(\frac{2}{C^2} - \frac{1}{C_s^2} \right) A_1 e^{-p\omega z} - \frac{2i\mu q}{C} B_1 e^{-q\omega z} \right] e^{i\omega(x/C-t)}, \quad (8)$$

$$\tau_{zx2} = \omega^2 \left[\frac{2i\mu p}{C} A_2 e^{p\omega z} - \mu \left(\frac{1}{C^2} + p^2 \right) B_2 e^{q\omega z} \right] e^{i\omega(x/C-t)},$$

$$\tau_{zz2} = \omega^2 \left[\mu \left(\frac{2}{C^2} - \frac{1}{C_s^2} \right) A_2 e^{p\omega z} + \frac{2i\mu q}{C} B_2 e^{q\omega z} \right] e^{i\omega(x/C-t)},$$

where λ and μ are the Lamé's constants.

By substituting (6) through (8) into the boundary conditions (equations (1)), the following four homogeneous, linear equations are obtained,

$$\frac{i(k_x + 2\mu\omega p)}{C} A_1 - \left(\frac{\mu\omega}{C_s^2} - \frac{2\mu\omega}{C^2} - qk_x \right) B_1 - \frac{ik_x}{C} A_2 + qk_x B_2 = 0, \quad (9a)$$

$$\left(\frac{\mu\omega}{C_s^2} - \frac{2\mu\omega}{C^2} - pk_z \right) A_1 + \frac{i(k_z + 2\mu\omega q)}{C} B_1 - pk_z A_2 - \frac{ik_z}{C} B_2 = 0, \quad (9b)$$

$$\frac{2ip}{C} (A_1 + A_2) + \left(\frac{1}{C^2} + q^2 \right) (B_1 - B_2) = 0, \quad (9c)$$

$$\left(\frac{1}{C_s^2} - \frac{2}{C^2} \right) (A_1 - A_2) + \frac{2iq}{C} (B_1 + B_2) = 0. \quad (9d)$$

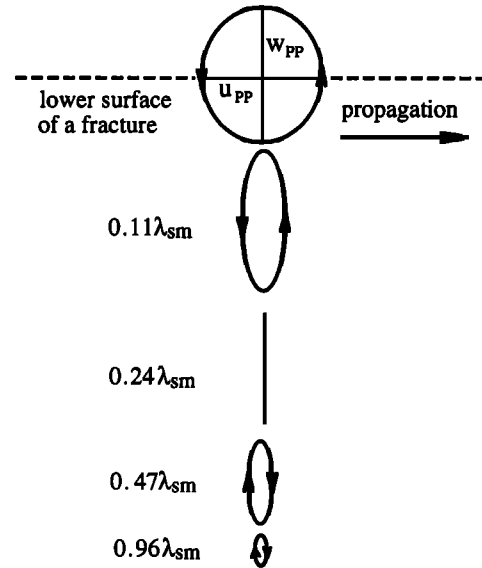
A comparison of displacements for the upper medium in (6) and those for the lower medium in (7) shows that when $B_2 = -B_1$ and $A_2 = A_1$, the wave field is symmetric with

respect to the fracture; and when $B_2 = B_1$ and $A_2 = -A_1$, the wave field is antisymmetric with respect to the fracture. The symmetric and antisymmetric wave fields are schematically shown in Figure 2. Substituting $B_2 = -B_1$ and $A_2 = A_1$ into (9) results in two linearly independent equations,

$$\frac{2ip}{C} A_1 + \left(\frac{1}{C^2} + q^2 \right) B_1 = 0,$$

$$\left(\frac{1}{C_s^2} - \frac{2}{C^2} - \frac{2pk_z}{\mu\omega} \right) A_1 + \frac{2i}{C} \left(\frac{k_z}{\mu\omega} + q \right) B_1 = 0. \quad (10)$$

a) a symmetric interface wave



b) an antisymmetric interface wave

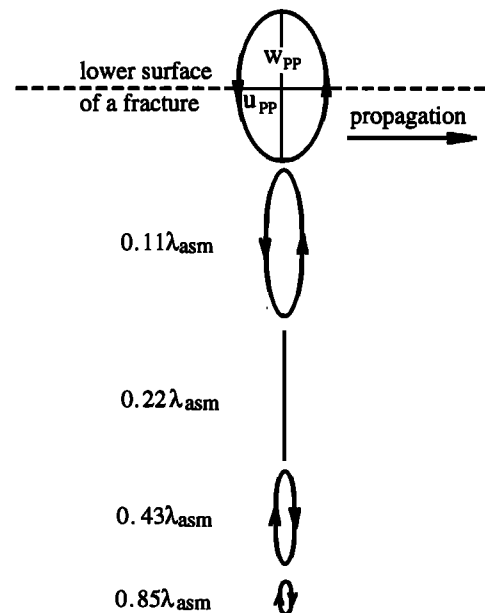


Figure 5. Particle motions of a symmetric and antisymmetric interface wave versus depth from a fracture when $C_p/C_s=1.53$ and the normalized fracture stiffness is assigned a value of 0.1. Symbols λ_{sm} and λ_{asm} are the wavelengths of the symmetric and antisymmetric interface waves, respectively.

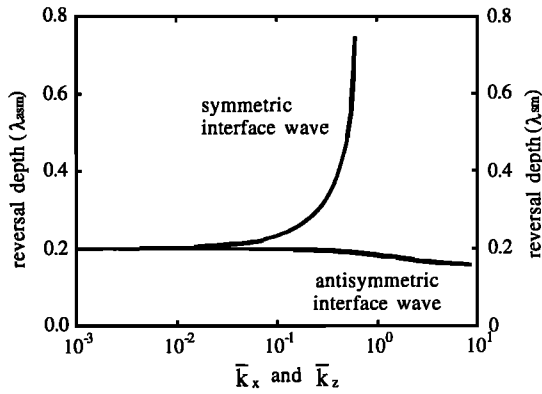


Figure 6. Reversal depths of the particle motion direction as a function of the normalized fracture stiffness for $C_P/C_S=1.53$. Symbols λ_{sm} and λ_{asm} are the wavelengths of the symmetric and antisymmetric interface waves, respectively.

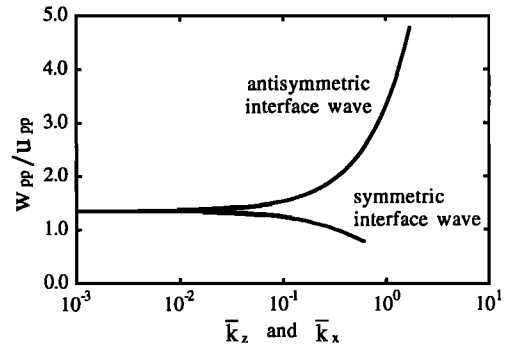


Figure 7. Radius ratios of the particle motion ellipse on the surfaces of a fracture as a function of the normalized fracture stiffness when $C_P/C_S=1.53$. Symbols w_{pp} and u_{pp} are the peak-peak amplitudes of the vertical and horizontal components, respectively, of the displacement on the fracture surface.

For a nontrivial solution of (10) to exist, the coefficient matrix of the two constants A_1 and B_1 must vanish, which yields an equation for the symmetric interface wave:

$$(1-2\xi^2)^2 - 4\xi^2\sqrt{\xi^2-\zeta^2}\sqrt{\xi^2-1} + 2\bar{k}_z\sqrt{\xi^2-\zeta^2} = 0, \quad (11)$$

where $\xi = C_S/C$, $\zeta = C_S/C_P$, and $\bar{k}_z = k_z/\omega Z_S$ ($Z_S = \rho C_S$ is the S wave impedance).

Similarly, substituting $B_2 = B_1$ and $A_2 = -A_1$ into (9), an equation for the antisymmetric interface wave is obtained,

$$(1-2\xi^2)^2 - 4\xi^2\sqrt{\xi^2-\zeta^2}\sqrt{\xi^2-1} + 2\bar{k}_x\sqrt{\xi^2-1} = 0, \quad (12)$$

where $\bar{k}_x = k_x/\omega Z_S$.

When the normalized fracture stiffnesses, \bar{k}_z and \bar{k}_x , are zero, both symmetric and antisymmetric interface wave equations (11) and (12) degenerate to the ordinary Rayleigh equation for a traction-free surface. However, when the normalized fracture stiffnesses are finite, (11) and (12), unlike the Rayleigh equation, contain wave frequency. Therefore the interface waves propagating along a fracture with a finite normalized stiffness are dispersive. The respective appearance of \bar{k}_z and \bar{k}_x in (11) and (12) indicates that the symmetric and antisymmetric interface waves are supported by the normal and tangential coupling between the surfaces of the fracture, respectively.

Using (11) and (12), the normalized phase velocities, C/C_S , of the symmetric and antisymmetric interface waves are calculated as a function of \bar{k}_z and \bar{k}_x for a range of C_P/C_S ratios and displayed in Figure 3. As \bar{k}_z and \bar{k}_x increase, the phase velocities of the two interface waves increase from the Rayleigh wave velocities to the shear wave velocity, with the symmetric interface wave propagating faster than the antisymmetric interface wave. Examination of the normalized fracture stiffness terms reveals that an increase in \bar{k}_z and \bar{k}_x can be induced by a decrease either in ω or Z_S or by an increase in k_z and k_x , respectively. Hence the increase of the normalized phase velocities of the interface waves with the normalized fracture stiffness can be a result of an increase in ω or Z_S or of an increase in k_z and k_x . By use of $v = 0.5(1-2\xi^2)/(1-\xi^2)$ where v is the Poisson's ratio,

it can be shown that the C_P/C_S values of 1.50, 1.63, 1.87, and 2.45 correspond to the Poisson's ratios of 0.1, 0.2, 0.3, and 0.4, correspondingly. Thus Figure 3 also shows that with increasing Poisson's ratio, the phase velocities of the interface waves increase relative to the S wave velocity for a given value of the normalized fracture stiffness.

The explanation for the increase of C/C_S with Poisson's ratio may be as follows. As Poisson's ratio increases, the velocity of the ordinary Rayleigh wave increases. Therefore the phase velocities of the interface waves accordingly increases because the interface waves are formed of coupling of two ordinary Rayleigh waves by the fracture stiffness.

It should be pointed out that the normalized phase velocities of the interface waves depicted in Figure 3 are obtained by searching for roots of (11) and (12) in the real domain. When the solution range is extended to the complex domain, a complex root of (11), that is, the leaky mode of the symmetric interface wave, is obtained for $\bar{k}_z > (\bar{k}_z)_{cf}$. The normalized phase velocities of the symmetric and antisymmetric interface waves, including the leaky mode of the symmetric interface wave, are shown in Figure 4 for $C_P/C_S=1.53$.

By setting $\xi = 1$ in (11), the normalized fracture stiffness which defines the boundary between the normal and leaky modes of the symmetric interface wave, $(\bar{k}_z)_{cf}$, can be found with the form

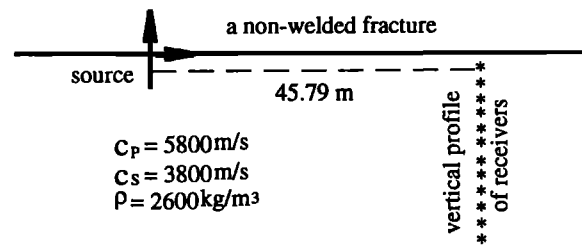
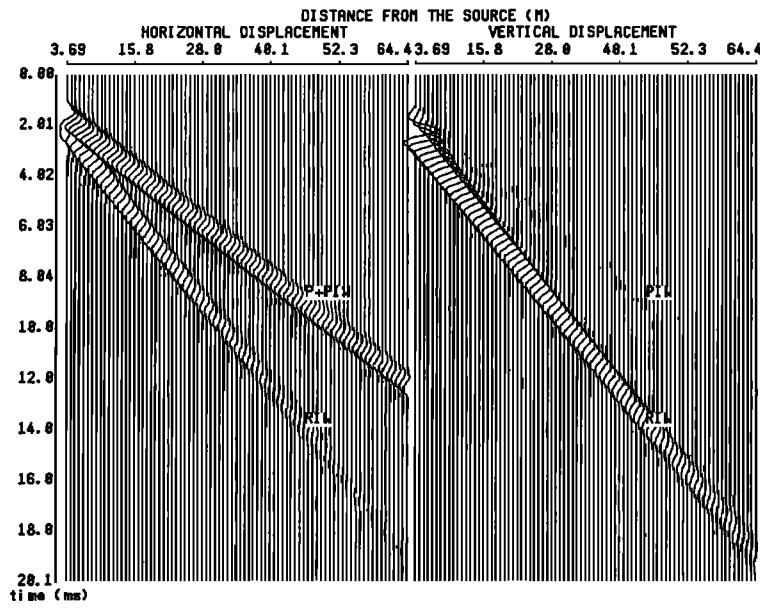


Figure 8. Simulation geometry used to generate symmetric and antisymmetric interface waves. The source line is perpendicular to the plane of the paper.

a) horizontal source, $k_z = 5 \times 10^9 \text{ Pa/m}$



b) vertical source, $k_x = 5 \times 10^9 \text{ Pa/m}$

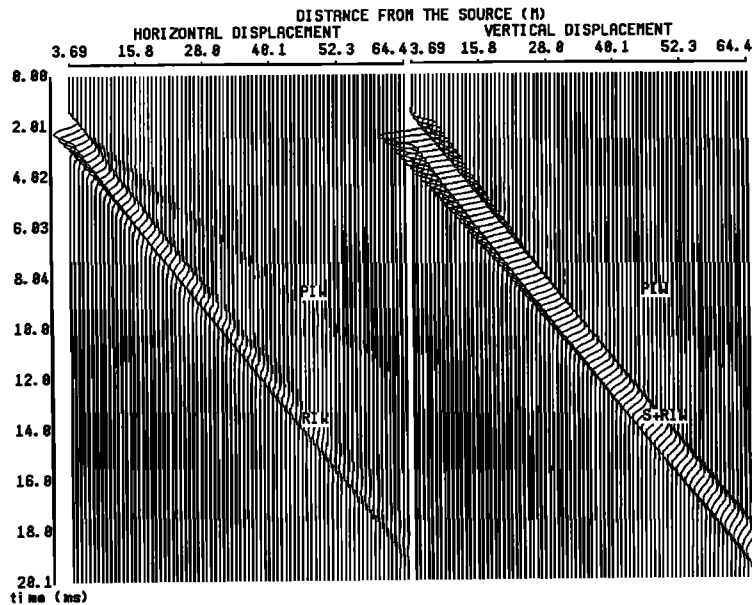


Figure 9. Seismic sections recorded along the lower surface of the fracture.

$$(\bar{k}_z)_{cf} = \frac{1}{2\sqrt{1-\zeta^2}}, \quad (13)$$

or

$$(\bar{k}_z)_{cf} = 0.5\sqrt{2(1-\nu)}, \quad (14)$$

by substituting $\zeta^2 = (1-2\nu)/(2-2\nu)$ into (13). Equations (13) and (14) give an expression for the cut-off normalized fracture stiffness for the symmetric interface wave. However, no cut-off normalized fracture stiffness is found to exist for the antisymmetric interface wave from (12). This demonstrates once again that the antisymmetric interface wave is nonleaky

for the whole range of normalized fracture stiffnesses (see also Figures 3 and 4).

Particle motions of the two interface waves for a normalized fracture stiffness of 0.1 and $C_p/C_s=1.53$ are plotted in Figure 5. The particle motions of both the symmetric and antisymmetric interface waves, like those in the Rayleigh wave field on a traction-free surface, exhibit elliptic trajectories and they are retrograde near the fracture and reverse to prograde at a certain depth. The reversal depth of particle motion direction is calculated as a function of the normalized fracture stiffnesses and is displayed in Figure 6. With increasing normalized fracture stiffness, the reversal

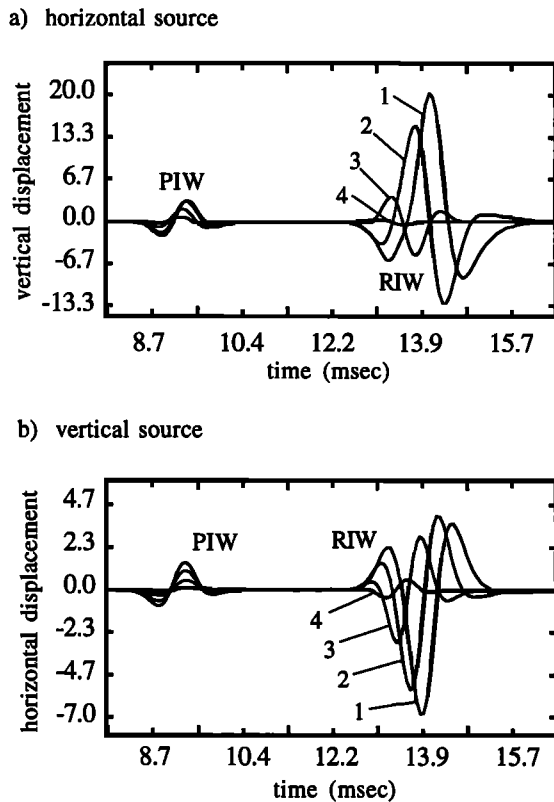


Figure 10. Waveforms recorded on the lower fracture surface, at distance 45.79 m from source. Fracture specific stiffnesses are (1) $k_z=10^9$, (2) $k_z=5 \times 10^9$, (3) $k_z=2.5 \times 10^{10}$, and (4) $k_z=10^{11}$ Pa/m in the horizontal source case, and (1) $k_x=5 \times 10^9$, (2) $k_x=10^{10}$, (3) $k_x=2.5 \times 10^{10}$ and (4) $k_x=10^{11}$ Pa/m in the vertical source case.

depth for the symmetric interface wave greatly increases while that for the antisymmetric interface wave slightly decreases.

Figure 5 also shows that the particle motion ellipse on the fracture surface is more vertically polarized for the antisymmetric interface wave than the one for the symmetric interface wave. The ratio of the ellipse radii of the particle motion, or equivalently, the ratio of the peak-peak amplitude of the vertical displacement to that of the horizontal displacement, on the fracture surface has been evaluated for a range of normalized fracture stiffnesses and displayed in Figure 7. The two curves in Figure 7 indicate that, with increasing the normalized fracture stiffness, the particle motion ellipse on the fracture surface becomes more horizontally polarized for the symmetric interface wave and more vertically polarized for the antisymmetric interface wave. This dependence of particle motion polarization on the symmetry of interface wave fields may be explained as follows. The symmetric interface wave is supported by only the normal component and not the tangential component of the normalized fracture stiffness (see (11)). Thus, as the normalized fracture stiffness increases, the symmetric interface wave is compressed in the normal direction and not in the tangential direction, which leads to the particle motion of the symmetric interface wave becoming more horizontally polarized. For the antisymmetric interface wave, the tangential component and not the normal component of the normalized fracture stiffness has an effect on it (see (12)). As

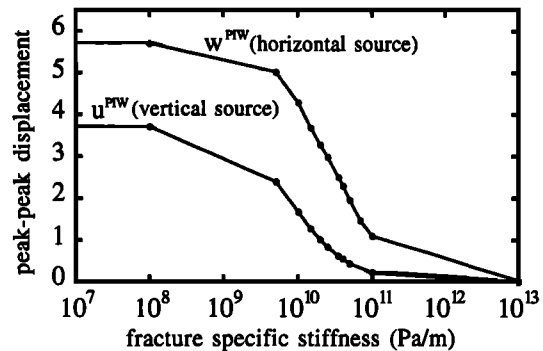
a result, as the normalized fracture stiffness increases, the particle motion ellipse of the antisymmetric interface wave becomes more vertically polarized because it is compressed only in the tangential direction and not in the normal direction.

Figures 3, 4, and 7 show that as $\bar{k}_x \rightarrow \infty$, the particle motion ellipse of the antisymmetric interface wave approaches an asymptote defined by the particle polarization of a body S wave propagating parallel to the fracture, and the velocity of the antisymmetric interface wave reaches the velocity of the S wave. With (6), (7), (10), and (11), it can be demonstrated that as $\bar{k}_x \rightarrow \infty$, the antisymmetric interface wave degenerates to a body S wave which propagates parallel to the fracture with the form

$$u_1 = u_2 = 0, \\ w_1 = w_2 = -B_1 \frac{\omega}{C_S} \sin \omega \left(\frac{x}{C_S} - t \right). \quad (15)$$

With increasing \bar{k}_z , the particle motion of the symmetric interface wave becomes more horizontally polarized (see Figure 7). As $\bar{k}_z \rightarrow \infty$, the phase velocity of the symmetric interface wave approaches the P wave velocity (see Figure 4). From (6), (7), (9), and (12), it has been derived that as $\bar{k}_z \rightarrow \infty$, the displacements for the symmetric interface wave become

a) *PIW* interface wave



b) *RIW* interface wave

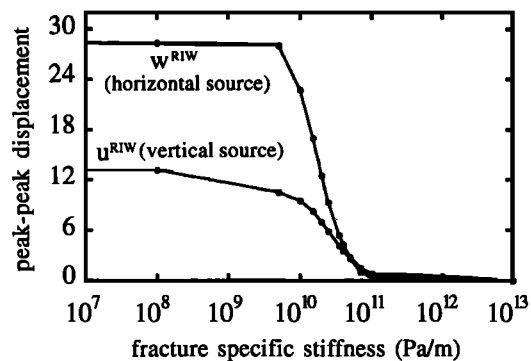


Figure 11. Peak-peak amplitudes of the *PIW* and *RIW* interface waves as a function of fracture specific stiffness. The range of the fracture specific stiffness from 10^7 to 10^{13} Pa/m in this figure corresponds to that of the normalized fracture stiffness from 0.2×10^{-3} to 0.2×10^3 .

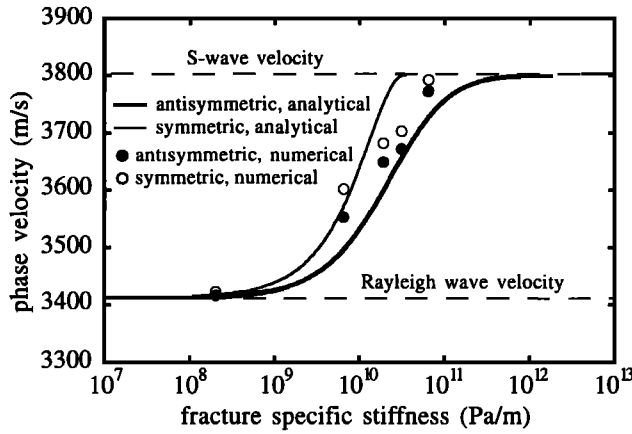


Figure 12. Phase velocities of the *RIW* interface waves as a function of fracture specific stiffness. The range of the fracture specific stiffness from 10^7 to 10^{13} Pa/m in this figure corresponds to that of the normalized fracture stiffness from 0.2×10^{-3} to 0.2×10^3 .

$$u_1 = u_2 = -A_1 \frac{\omega}{C_P} \sin \omega \left(\frac{x}{C_P} - t \right), \quad (16)$$

$$w_1 = w_2 = 0.$$

This indicates that the symmetric interface wave degenerates to a body *P* wave that propagates parallel to the fracture as $\bar{k}_z \rightarrow \infty$.

Line Source Analysis

Interface waves along a fracture generated by a line source at the fracture are investigated using a boundary element method (BEM). In the BEM scheme, the upper and lower fracture surfaces are divided into quadratic boundary elements. The time variable is discretized using an implicit time-stepping algorithm. The displacement discontinuity boundary conditions given in (1) are applied between the upper and lower surfaces of a fracture. A system of linear equations is then formed, which is used to solve for unknown displacements and stresses on the surfaces of the fracture. The displacements in the two half-spaces are computed afterward by direct use of the dynamic integral representation. Details of the BEM for a fractured medium have been given by *Gu et al.* [1994].

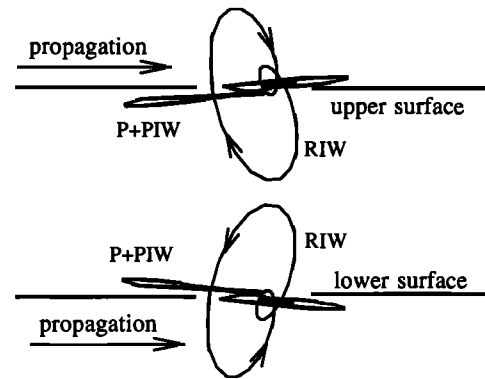
In the following, numerical experiments are conducted for the model geometry shown in Figure 8. The two elastic half-spaces are assigned *P* and *S* wave velocities and a density, $C_P = 5800$ m/s, $C_S = 3800$ m/s and $\rho = 2600$ kg/m³, respectively. The source is a three-lobe Ricker wavelet with a central frequency of 800 Hz.

Figure 9 displays two seismic sections recorded on the lower surface of the fracture. The four arrivals observed are labeled u^{P+PIW} , w^{PIW} , u^{RIW} and w^{RIW} in the horizontal source case and u^{PIW} , w^{PIW} , u^{RIW} and w^{S+RIW} in the vertical source case. Here superscripts *PIW* and *RIW* indicate, respectively, *P*-type and Rayleigh-type interface waves, *P+PIW* denotes a mixture of a body *P* wave and a *PIW* interface wave, and *S+RIW* refers to a mixture of a body *S* wave and a *RIW* interface wave. The mixing of the interface waves and the body waves is because the fracture used in the

numerical simulations is not long enough for the two waves to separate from each other. Clearly, there exist on the surface of the fracture only u^P in the horizontal source case and w^S in the vertical source case when the fracture is completely welded. Hence, w^{PIW} , u^{RIW} and w^{RIW} in the horizontal source case and u^{PIW} , w^{PIW} , and u^{RIW} in the vertical source case are generated due to the finite stiffness of the fracture and are interface waves.

To examine the effects of the fracture specific stiffness on the interface waves, displacements recorded on the lower fracture surface, 45.79 m from the source, are displayed in Figure 10 for a range of fracture specific stiffnesses. Both the shape and amplitude of the waveforms vary with fracture specific stiffness.

a) symmetric interface wave



b) antisymmetric interface wave

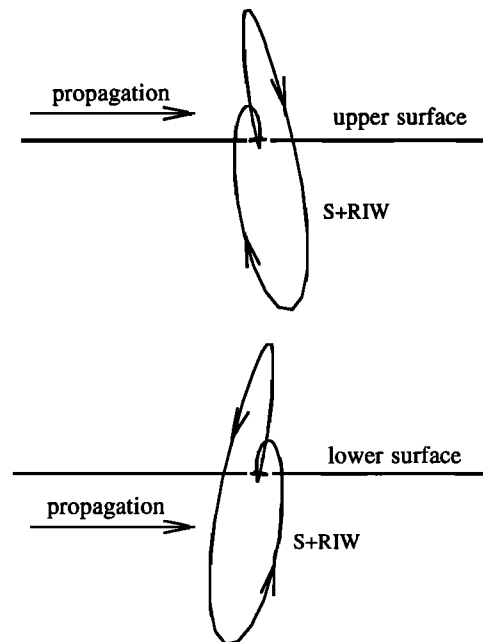


Figure 13. Particle motions on the upper and lower surfaces of the fracture, at distance 45.79 m from source.

Figure 11 shows that the peak-peak amplitudes of the displacements for the *PIW* and *RIW* interface waves decrease as the fracture specific stiffness increases, which indicates that less seismic energy is partitioned from body waves into the interface waves with increasing fracture specific stiffness.

Figure 12 displays the phase velocities of the *RIW* interface waves versus fracture specific stiffness. The analytical phase velocities are calculated using the symmetric and antisymmetric interface equations (11) and (12). The numerical phase velocities of the symmetric and antisymmetric interface waves are obtained by calculating $14.82\omega/\Delta\theta$ for a line source at the fracture, where $\Delta\theta$ is the phase difference of a Fourier component of the interface waves recorded on the fracture surface at distance 29.83 m and 44.65 m from the sources and the angular frequency of the Fourier component $\omega = 2\pi * 690$ Hz. The numerical and analytical velocities are basically consistent with each other although there is some discrepancy between them. The discrepancy is induced, most probably, by the use of not-fine-enough grids and time intervals for the numerical simulations.

Figure 13 shows particle motions of the symmetric and antisymmetric interface waves observed on the upper and lower fracture surfaces, 45.79 m from the source, for the geometry shown in Figure 8. The symmetric and antisymmetric interface waves are generated by the horizontal and vertical sources, respectively. The fracture is assigned a specific stiffness of $k_z = 5 \times 10^9$ Pa/m in the symmetric case and $k_x = 5 \times 10^9$ Pa/m in the antisymmetric case. The particle motions of the *RIW* interface waves on both the upper and lower surfaces of the fracture are retrograde.

Figure 14 shows particle motions recorded along the vertical receiver profile in the lower medium for the horizontally polarized source case shown in Figure 8. The *P+PIW* wave traces out largely horizontally polarized particle motions, and the *S+RIW* and *RIW* waves trace out more vertically polarized particle motions. The particle motion of the *S+RIW* wave reverses from retrograde to prograde at depth $0.17 \lambda_S$ (S wavelength) from the fracture. The particle motion of the *P+PIW* wave, opposite in particle motion direction to the *S+RIW* wave, changes from prograde near the fracture to retrograde at depth $0.17 \lambda_P$ (P wavelength) from the fracture. Now, the vertical component of the *P+PIW* wave, instead of the horizontal component of the *S+RIW* wave, goes through zero at depth $0.17 \lambda_P$ from the fracture. The vertical displacement of the *P+PIW* wave reaches a maximum, not on the fracture surface, but at a slight depth, around $0.06 \lambda_P$ away from the fracture. Deeper than $1.18 \lambda_S$ from the fracture, the *PIW* and *RIW* interface waves disappear and the body waves dominate.

Summary and Conclusions

An extensive fracture in a solid can be modeled for seismic waves as a displacement discontinuity boundary condition between the surfaces of the fracture. Across the fracture, seismic stresses are continuous and particle displacements are discontinuous by an amount which is proportional to the stresses and inversely proportional to the mechanical specific stiffness of the fracture. Based on the fracture model, interface waves along a single, extensive fracture in an elastic solid were investigated using plane wave analysis and a boundary element method.

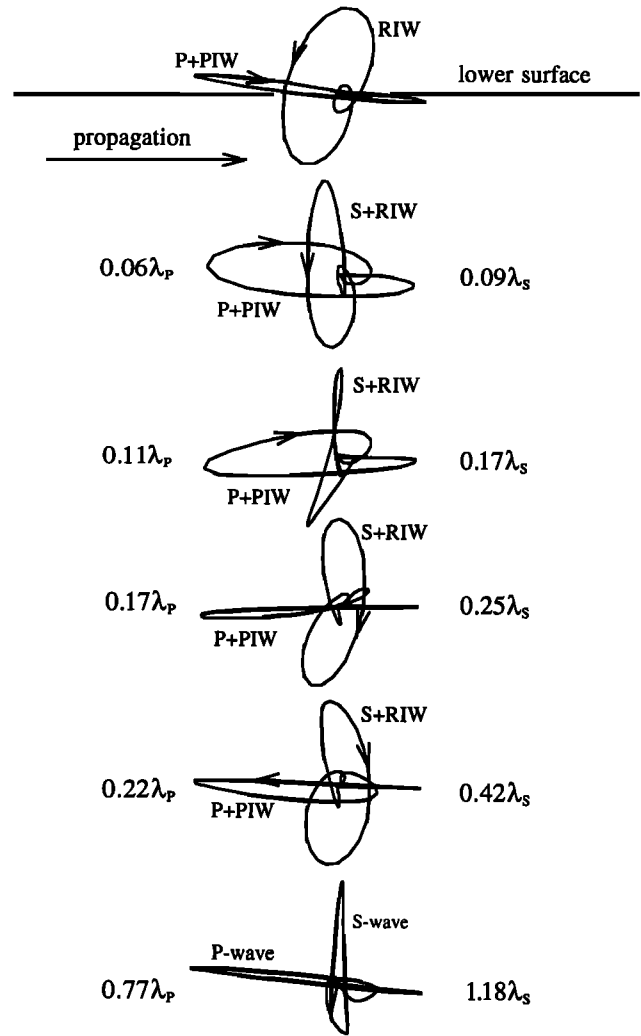


Figure 14. Particle motions observed along the vertical profile for the horizontally polarized source (see Figure 8). The fracture is assigned a specific stiffness of $k_z = 5 \times 10^9$ Pa/m. The depth is normalized by the P and S wavelengths, λ_P and λ_S .

In the plane wave analysis, the displacement discontinuity boundary condition for a fracture was applied to the potentials for the displacement field of inhomogeneous plane waves. This directly results in a 4 by 4 matrix equation for interface waves. By considering the symmetry of the wave field with respect to the fracture, the 4 by 4 matrix equation is decomposed into two 2 by 2 matrices which give the symmetric and antisymmetric interface wave equations. The normalized fracture stiffness (which is the ratio of the fracture specific stiffness to the product of the wave's angular frequency and the S wave impedance of the two half-spaces) controls the behavior of the interface waves. The normal and tangential components of the normalized fracture stiffness support the symmetric and antisymmetric interface waves, respectively. As the normalized fracture stiffness increases from lower to higher values, the phase velocities of the symmetric and antisymmetric interface waves increase from the Rayleigh wave velocity to the velocities of the body P and S waves, respectively. For values of the normalized fracture

stiffness above $0.5\sqrt{2(1-\nu)}$ (ν is Poisson's ratio), the symmetric interface wave exists in a leaky mode.

In the wave field near a fracture generated by a line source, a P -type interface wave is observed to exist in addition to the Rayleigh-type interface waves predicted by the plane analysis. The particle motion of the RIW interface wave reverses from retrograde near the fracture to prograde at a certain depth. The particle motion direction of the PIW interface wave, opposite to the particle motion direction of the RIW interface wave, changes from prograde near the fracture to retrograde at a certain depth. With decreasing fracture specific stiffness, more seismic energy is partitioned from body waves into the interface waves.

These results may find direct application to seismic detection and characterization of fractures in the field. Interface waves are characterized by localization of the seismic energy in the neighborhood of the fracture and hence travel with less loss in amplitude along the fracture than body waves which spread in three dimensions. In addition, fracture interface waves directly sample the mechanical properties of fractures. Therefore interface wave techniques may become a quantitative diagnostic tool for evaluating the physical properties of fractures in geoenvironment and the strength of welding, bonds, and adhesives in nondestructive testing. For example, the leaky mode of the symmetric interface wave allows fractures to be detected by receivers located off the fracture. The dependence of the interface waves on the components of fracture stiffness may allow separate estimates of the horizontal and vertical components of fracture stiffness.

Acknowledgments. The work was supported by the Director, Office of Energy Research, Office of Basic Energy Sciences under U.S. Department of Energy Contracts DE-AC03-76SF00098 and DE-F602-93ER14391.

References

- Brown, S.R., and C.H. Scholz, Closure of random surfaces in contact, *J. Geophys. Res.*, **90**, 5531-5545, 1985.
- Cook, N.G.W., Natural joints in rock: Mechanical hydraulic and seismic behavior and properties under normal stress, *Int. J. Rock Mech. Min. Sci. Geomech. Abstr.*, **29**, 188-223, 1992.
- Gangi, A.F., Variation of whole- and fractured-porous-rock permeability with confining pressure, *Int. J. Rock Mech. Min. Sci. Geomech. Abstr.*, **57**, 249-257, 1978.
- Greenwood, J.A., and J.B.P. Williamson, Contact of nominally flat surfaces, *Proc. R. Soc. London, A*, **295**, 300-318, 1966.
- Gu, B., N.G.W. Cook, K.T. Nihei, and L.R. Myer, Modeling elastic wave propagation in a medium with non-welded interfaces using the boundary integral equation method, in *Computer Methods and Advances in Geomechanics*, edited by H.J. Siriwardane, and M.M. Zaman, pp. 387-392, A.A. Balkema, Brookfield, Vt., 1994.
- Hopkins, D.L., N.G.W. Cook, and L.R. Myer, Fracture stiffness and aperture as a function of applied stress and contact geometry, *Proc. U.S. Symp. Rock Mech.*, **29th**, 673-680, 1987.
- Kendall, K., and D. Tabor, An ultrasonic study of the area of contact between stationary and sliding surfaces, *Proc. R. Soc. London, A*, **1323**, 321-340, 1971.
- Murty, G.S., A theoretical model for the attenuation and dispersion of Stoneley waves at the loosely bonded interface of elastic half-space, *Phys. Earth Planet Inter.*, **11**, 65-79, 1975.
- Myer, L.R., D.L. Hopkins, and N.G.W. Cook, Effects of contact area of an interface on acoustic wave transmission characteristics, *Pro. U.S. Rock Mech. Symp.*, **26th**, 565-572, 1985.
- Pyrak-Nolte, L.J., and N.G.W. Cook, Elastic interface waves along a fracture, *Geophys. Res. Lett.*, **14**, 1107-1110, 1987.
- Pyrak-Nolte, L.J., L.R. Myer, and N.G.W. Cook, Transmission of seismic waves across natural fractures, *J. Geophys. Res.*, **95**, 8617-8638, 1990.
- Pyrak-Nolte, L.J., J. Xu, and G.M. Haley, Elastic interface waves propagating in a fracture, *Phys. Rev. Lett.*, **68**, 3650-3653, 1992.
- Rokhlin, S., Adhesive joint characterization by ultrasonic surface and interface wave, in *Adhesive Joints*, edited by K.L. Mittal, Plenum, New York, 307-345, 1984.
- Rokhlin, S.I., and Y.J. Wang, Analysis of boundary conditions for elastic wave interaction with an interface between two solids, *J. Acoust. Soc. Am.*, **89(2)**, 503-515, 1991.
- Schoenberg, M., Elastic wave behavior across linear slip interfaces, *J. Acoust. Soc. Am.*, **68**, 1516-1521, 1980.
- Xu, P.C., and S.K. Datta, Guided waves in a bonded plate: A parametric study, *J. Appl. Phys.*, **67**, 6779-6789, 1990.
- B. Gu, L.R. Myer, and K.T. Nihei, Earth Sciences Division, Lawrence Berkeley Laboratory, Bldg 50E, 1 Cyclotron Road, Berkeley, CA 94720. (e-mail: boliang@jard.lbl.gov)
- L.J. Pyrak-Nolte, Department of Civil Engineering and Geological Sciences, University of Notre Dame, Notre Dame, IN 46556.

(Received February 6, 1995; revised September 5, 1995; accepted September 13, 1995)